



# Synthesis of Magnetic Chitosan-Fly Ash/Fe<sub>3</sub>O<sub>4</sub> Composite for Adsorption of Reactive Orange 16 Dye: Optimization by Box–Behnken Design

Ali H. Jawad<sup>1</sup> · Nurul Najwa Abd Malek<sup>1</sup> · Ahmed Saud Abdulhameed<sup>2</sup> · R. Razuan<sup>1</sup>

Published online: 3 February 2020

© Springer Science+Business Media, LLC, part of Springer Nature 2020

## Abstract

A hybrid composite biopolymer of magnetic chitosan-fly ash/Fe<sub>3</sub>O<sub>4</sub> (CS-FA/Fe<sub>3</sub>O<sub>4</sub>) was prepared to be an effective composite biosorbent for the removal of reactive orange 16 (RO16) dye from aqueous media. Various analytical techniques such as XRF, BET, XRD, FTIR, and SEM–EDX were utilized to characterize of CS-FA/Fe<sub>3</sub>O<sub>4</sub> composite. The effects of adsorption process parameters namely adsorbent dose (A: 0.04–0.12 g), solution pH (B: 4–10), temperature (C: 30–50 °C), and time (E: 20–90 min) were optimized by using Box–Behnken design (BBD) in response surface methodology (RSM). The experimental results indicate that the highest RO16 removal was 73.1% by significant interaction between BC (p-value = 0.0002) and AD (p-value = 0.022). The optimum RO16 dye removal conditions were recorded at solution pH ~ 4, adsorbent dose (0.08 g), temperature (30 °C), and time (55 min). The adsorption process was well described by pseudo-second order (PSO) kinetic and Freundlich isotherm model. The adsorption capacity of CS-FA/Fe<sub>3</sub>O<sub>4</sub> composite for RO16 dye was 66.9 mg/g at 30 °C. The mechanism of the RO16 dye adsorption included many interactions such as electrostatic, n–π interaction, H-bonding, and Yoshida H-bonding. Furthermore, the CS-FA/Fe<sub>3</sub>O<sub>4</sub> composite exhibited a high ability to separate from the aqueous solution after adsorption process by external magnetic field.

**Keywords** Magnetic chitosan · Fly ash · Reactive orange 16 dye · Adsorption · Response surface methodology

## Introduction

Organic dyes are widely utilized in various industries such as printing, textile, leather, paint, and pharmaceuticals [1]. The discharge of these dyes without treatment into water is one of the environmental problems due to its risks on aquatic life and human's health [2]. Therefore, it is necessary to remove these dyes before releasing it into the environment. Several methods have been applied to remove these dyes prior to discharge into water such as photocatalytic [3], adsorption [4, 5], oxidation [6], and flocculation [7]. Adsorption is considered one of the most efficient methods used to remove

dyes because of the simplicity of design, non-generation of toxic materials, low cost, and high efficiency [8–10].

Chitosan (CS) is a cationic polysaccharide composed of D-glucosamine units [11]. CS can be obtained from the deacetylation of chitin, which is the second most abundant biopolymer in nature after cellulose [12]. CS has various interesting properties such as biodegradability, non-toxicity, biocompatibility, and antimicrobial activity [13, 14]. The uniqueness of CS molecular structure comes from the availability of amino (–NH<sub>2</sub>) and hydroxyl (–OH) groups [15], which are represented active adsorption sites for the removal several of water pollutants such as dyes [16] and metal ions [17]. However, the application of natural CS as a biosorbent in wastewater treatment technologies still limited due to the high swelling index, solubility in various organic acids, low surface area, and considerable leachability [18].

In general, various successful treatment methods are frequently applied to enhance the chemical and structural characteristics of CS such as crosslinking reaction, which is convenient and feasible pathway to reduce its solubility in acidic medium and to minimize the hydrophobicity

✉ Ali H. Jawad  
ali288@uitm.edu.my; ahjm72@gmail.com

<sup>1</sup> Faculty of Applied Sciences, Universiti Teknologi MARA, 40450 Shah Alam, Selangor, Malaysia

<sup>2</sup> Chemistry Department, College of Science, University of Anbar, Ramadi, Iraq

and swelling index in aqueous solution [19]. However, the crosslinking reaction generally leads to decrease the adsorption capacity of CS due to blocking its reactive adsorption sites, particularly amino ( $-\text{NH}_2$ ) group when react with dialdehyde crosslinker agent [20]. To overcome this drawback, fabricating CS nanocomposite materials is another promising pathway for enhancing the structural and surface area of CS biopolymer and reducing its internal diffusion resistance [19]. Therefore, various promising materials with multifunctional groups such as  $\text{TiO}_2$  nanoparticles, clays, and fly ash particles were incorporated into molecular structure of CS to improve its adsorptive and physiochemical properties [21–23].

In this respect, fly ash (FA) is a by-product generated from combusting of coal in the thermal power plants [24]. The FA contains mainly of metal oxides such as silica ( $\text{SiO}_2$ ), alumina ( $\text{Al}_2\text{O}_3$ ), and magnetite ( $\text{Fe}_2\text{O}_3$ ), in addition to unburned carbon [25, 26]. FA has many preferable properties to be promising adsorbent such as chemical composition, surface area, porosity, particle size, and water holding capacity [23]. However, the main technical drawbacks of using bare FA as an adsorbent in wastewater treatment technologies were due to the difficulty of filtration and separation processes of ultrafine particles from treated solution during and post treatment process. Recently, the FA and/or CS-FA composite were applied as adsorbents for removal of organic water pollutants from contaminated water [27, 28].

Moreover, magnetic nanoparticles (such as  $\text{Fe}_3\text{O}_4$  and  $\text{Fe}_2\text{O}_3$ ) were introduced as the magnetic core within composite adsorbent in order to achieve the effective separation and easy collection of adsorbents from aqueous media by external magnetic field [29, 30].  $\text{Fe}_3\text{O}_4$  nanoparticles were widely utilized in preparation of adsorbents due to its exceptional features such as surface functional groups, magnetic response ability, small particle size, biocompatibility, and biodegradability [31]. Recently, magnetic CS- $\text{Fe}_3\text{O}_4$  composites were widely prepared and used as adsorbents in adsorption technique for removal of dyes [32], pharmaceuticals [33], and metal ions [34].

Therefore, the main objective of this research work was to produce multifunctional performances of recoverable and separable composite magnetic chitosan-fly ash/ $\text{Fe}_3\text{O}_4$  (CS-FA/ $\text{Fe}_3\text{O}_4$ ) as an effective biosorbent to remove of reactive orange 16 (RO16) dye from aqueous media. The key parameters affecting the RO16 dye adsorption such as adsorbent dose, solution pH, temperature, and time were optimized using Box–Behnken design (BBD) in response surface methodology (RSM). Furthermore, the non-linear forms of isotherm and kinetic models were studied. Finally, a suitable mechanism for RO16 dye adsorption by CS-FA/ $\text{Fe}_3\text{O}_4$  composite was proposed.

## Materials and Methods

### Materials

The fly ash (FA) was collected from thermal power station situated in Kapar area, Selangor, Malaysia. FA powder was washed with distilled water to remove any soluble substances. Then, FA powder was dried in an oven at 80 °C for 24 h before sieving to certain particles size  $\leq 250 \mu\text{m}$ . CS (deacetylation  $\geq 75\%$ ; medium molecular weight) was obtained from Sigma-Aldrich. Iron(III) chloride hexahydrate ( $\text{FeCl}_3 \cdot 6\text{H}_2\text{O}$ , MW: 270.30 g/mol) was purchased from HmbG Chemicals. Iron(II) chloride tetrahydrate ( $\text{FeCl}_2 \cdot 4\text{H}_2\text{O}$ , MW: 198.81 g/mol) was purchased from Bendosen Laboratory Chemicals. Reactive orange 16 dye ( $\text{C}_{20}\text{H}_{17}\text{N}_3\text{Na}_2\text{O}_{11}\text{S}_3$ , MW: 617.54 g/mol,  $\lambda_{\text{max}} = 493 \text{ nm}$ ) was purchased from ACROS, Organics. Acetic acid, Hydrochloric acid, and sodium hydroxide were supplied from R&M Chemicals. All experiments of this research were performed using ultrapure water.

### Synthesis of Magnetic Chitosan-Fly Ash/ $\text{Fe}_3\text{O}_4$ Composite (CS-FA/ $\text{Fe}_3\text{O}_4$ )

1 g of CS flakes and 1 g of FA particles were blended in acetic acid solution (5%, 50 mL). The solution was slowly stirred for 24 h at 25 °C to ensure dissolution of CS flakes and loading of FA particles in the CS molecular structure. After that, 10 mL containing 0.014 mol of  $\text{Fe}^{3+}$  ions and 0.013 mol of  $\text{Fe}^{2+}$  ions (these ions were prepared by dissolving 3.9 g of  $\text{FeCl}_3 \cdot 6\text{H}_2\text{O}$  and 2.7 g of  $\text{FeCl}_2 \cdot 4\text{H}_2\text{O}$  in distilled water) were added to the solution of CS-FA with gentle stirring for 1 h at 25 °C. The obtained solution was injected into of sodium hydroxide solution (2 M, 1000 mL) by syringe needle (10 mL) with gentle stirring for 6 h, where the magnetic CS-FA/ $\text{Fe}_3\text{O}_4$  beads were instantaneously formed. The fresh beads of magnetic CS-FA/ $\text{Fe}_3\text{O}_4$  were washed using distilled water to remove the residue of sodium hydroxide solution. Then, the CS-FA/ $\text{Fe}_3\text{O}_4$  powder (particle size  $\leq 250 \mu\text{m}$ ) was achieved by grinding process of CS-FA/ $\text{Fe}_3\text{O}_4$  beads. The synthesis steps of CS-FA/ $\text{Fe}_3\text{O}_4$  and image of CS-FA/ $\text{Fe}_3\text{O}_4$  beads are presented in Fig. 1.

### Characterization

The characterization of CS-FA/ $\text{Fe}_3\text{O}_4$  composite was performed by various analytical methods and techniques. The chemical composition of FA was determined by X-ray Fluorescence (XRF) analysis. The surface area and pore volume of the CS-FA/ $\text{Fe}_3\text{O}_4$  composite was determined by Micromeritics ASAP 2060 analyzer using

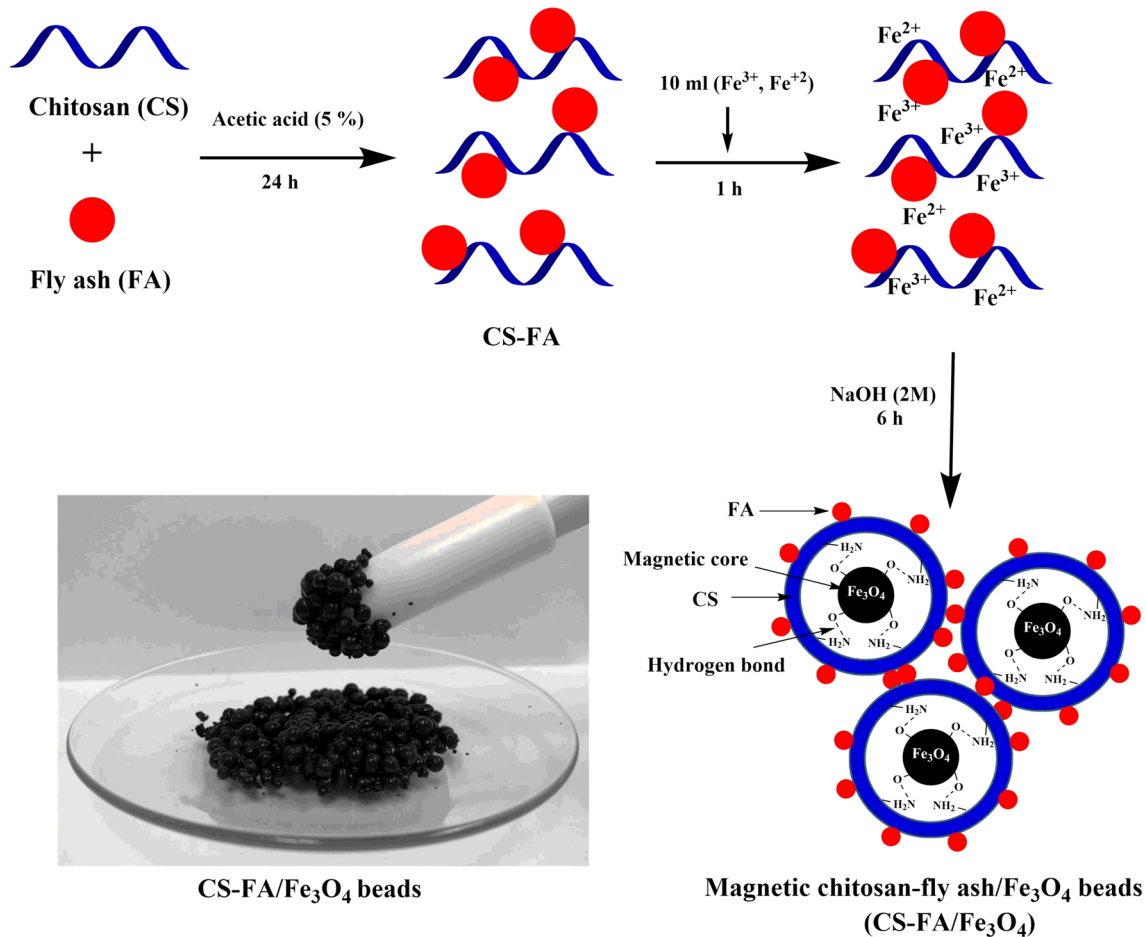


**Fig. 1** The synthesis steps of CS-FA/Fe<sub>3</sub>O<sub>4</sub> composite

nitrogen adsorption/desorption isotherms at 77 K. Scanning electron microscope-energy dispersive X-ray analyze (SEM-EDX, Zeiss Supra 40 VP, Germany) was utilized to determine the morphological characteristics of CS-FA/Fe<sub>3</sub>O<sub>4</sub> composite before and after adsorption of RO16 dye molecules. The X-Ray diffraction (XRD, X'Pert PRO, PANalytical) was used to determine the crystallinity of CS-FA/Fe<sub>3</sub>O<sub>4</sub> composite. pH-potentiometric titration was performed to determine the amine content in CS-FA/Fe<sub>3</sub>O<sub>4</sub> composite based on the method published by Vieira and Beppu [35]. The point of zero charge (pH<sub>pzc</sub>) for CS-FA/Fe<sub>3</sub>O<sub>4</sub> composite was calculated based on the reported method [36]. The surface functional groups of CS-FA/Fe<sub>3</sub>O<sub>4</sub> composite before and after RO16 dye adsorption were determined using Fourier Transform Infrared (FTIR) spectroscopy (Perkin-Elmer, Spectrum RX I).

### Design of Experiments

Four independent variables namely adsorbent dose (A), solution pH (B), temperature (C), and time (D) were

optimized by using Box-Behnken design (BBD) in response surface methodology (RSM) for the RO16 dye adsorption onto CS-FA/Fe<sub>3</sub>O<sub>4</sub> composite. Design-Expert software (version 11, Stat-Ease, Minneapolis, USA) was used to design of experiments and analysis of the experimental results. The levels and ranges of independent variables and their codes are shown in Table 1. A second-order polynomial model was utilized to estimate the RO16 dye removal as presented in the following Eq. (1).

$$Y = \beta_0 + \sum \beta_i X_i + \sum \beta_{ii} X_i^2 + \sum \sum \beta_{ij} X_i X_j \quad (1)$$

**Table 1** Codes and actual variables and their levels in BBD

Codes	Variables	Level 1 (-1)	Level 2 (0)	Level 3 (+1)
A	Adsorbent dose (g)	0.04	0.08	0.12
B	pH	4.0	7.0	10
C	Temperature (°C)	30	40	50
D	Time (min)	20	55	90

where,  $Y$  is the response (dye removal),  $\beta_0$  is the model constant,  $\beta_i$  is the linear coefficient of the input parameter,  $\beta_{ii}$  is the quadratic coefficient of the input parameter, and  $\beta_{ij}$  is the interaction coefficient between the input parameters, while  $X_i$  and  $X_j$  represent the independent variables. A total of 29 experiments (runs) are designed by BBD to optimize and evaluate the four independent variables including A: adsorbent dose (0.04–0.12 g), B: solution pH (4–10), C: temperature (30–50 °C), and D: time (20–90 min) on the RO16 dye removal. Noteworthy, the ranges and levels for BBD-RSM were pre-determined to be the best. The actual experimental design and values of RO16 dye removal are given in Table 2. A certain amount of CS-FA/Fe<sub>3</sub>O<sub>4</sub> composite was

**Table 2** The 4-variables BBD matrix and experimental data for RO16 removal efficiency

Run	A: Adsorbent dose (g)	B: pH	C: Temp (°C)	D: Time (min)	RO16 removal (%)
1	0.04	4	40	55	45.0
2	0.12	4	40	55	62.6
3	0.04	10	40	55	15.2
4	0.12	10	40	55	23.5
5	0.08	7	30	20	25.5
6	0.08	7	50	20	10.2
7	0.08	7	30	90	35.0
8	0.08	7	50	90	22.4
9	0.04	7	40	20	7.90
10	0.12	7	40	20	13.6
11	0.04	7	40	90	12.4
12	0.12	7	40	90	45.2
13	0.08	4	30	55	73.1
14	0.08	10	30	55	16.2
15	0.08	4	50	55	25.7
16	0.08	10	50	55	22.2
17	0.04	7	30	55	15.9
18	0.12	7	30	55	32.7
19	0.04	7	50	55	14.7
20	0.12	7	50	55	33.3
21	0.08	4	40	20	36.3
22	0.08	10	40	20	15.8
23	0.08	4	40	90	48.6
24	0.08	10	40	90	17.2
25	0.08	7	40	55	15.2
26	0.08	7	40	55	14.8
27	0.08	7	40	55	15.9
28	0.08	7	40	55	14.6
29	0.08	7	40	55	15.4

added to the Erlenmeyer flasks (125 mL) containing RO16 dye solution (50 mL). These flasks were agitated at fixed shaking speed of 100 strokes/min using water bath (WNB7-45, Memmert, Germany). After that, the adsorbents were separated by an external magnetic field and the solution was filtered by syringe filter (0.45 μm). Finally, the concentrations of RO16 dye were calculated by UV–Vis spectroscopy (HACH DR 2800) at  $\lambda_{\max}$  493 nm. The RO16 dye removal (DR%) was calculated using the following Eq. (2).

$$DR\% = \frac{(C_o - C_e)}{C_o} \times 100 \quad (2)$$

where  $C_o$  (mg/L) is the RO16 dye initial concentration and  $C_e$  (mg/L) is the concentration of the RO16 dye at equilibrium.

The adsorptive removal of RO16 dye by bare fly ash powder (FA), CS/Fe<sub>3</sub>O<sub>4</sub>, and CS-FA/Fe<sub>3</sub>O<sub>4</sub> composite was pre-determined and compared. The RO16 dye removal was 28.9%, 39.9%, and 68.2% for the fly ash powder (FA), CS/Fe<sub>3</sub>O<sub>4</sub>, and CS-FA/Fe<sub>3</sub>O<sub>4</sub> composite adsorbents, respectively. This results show clearly the synergistic effect of incorporating FA powder into polymeric matrix of CS/Fe<sub>3</sub>O<sub>4</sub> on the adsorptive property of the composite CS-FA/Fe<sub>3</sub>O<sub>4</sub> for removal of RO16 dye.

### Batch Adsorption Study

The RO16 dye adsorption onto CS-FA/Fe<sub>3</sub>O<sub>4</sub> composite was studied in batch mode. According to Table 2 containing values of RO16 dye removal efficiency, the highest RO16 dye removal (%) can be obtained from run 13 under the following conditions: adsorbent dose (A: 0.08 g/L), pH (B: 4), temperature (C: 30 °C), and time (D: 55 min). Thus, these optimum conditions of adsorption key parameters were kept constant in the experiments of batch adsorption study. Adsorption experiments of RO16 dye were carried out using the same procedure mentioned above at different RO16 dye initial concentrations (20–150 mg/L) and contact time (0–660 min). The adsorption capacity of CS-FA/Fe<sub>3</sub>O<sub>4</sub> composite for RO16 dye at equilibrium,  $q_e$  (mg/g) was determined according to the following Eq. (3).

$$q_e = \frac{(C_o - C_e)V}{W} \quad (3)$$

where,  $V$  (L) is volume of RO16 dye solution and  $W$  (g) is the weight of CS-FA/Fe<sub>3</sub>O<sub>4</sub> composite. Adsorption experiments were conducted in duplicate under identical conditions and the results are reported as an average value.

## Results and Discussion

### Characterization

#### Physicochemical Properties

The elemental composition of FA was determined by XRF analysis and presented in Table 3. The result of analysis indicates the presence of Si, P, K, Ca, Al, Fe, Ti, Ag, Sr, and Zr mainly in structure of FA. Thus, it can be concluded that FA consist of metal oxides such  $\text{SiO}_2$ ,  $\text{Al}_2\text{O}_3$ ,  $\text{Fe}_2\text{O}_3$ ,  $\text{CaO}$ ,  $\text{TiO}_2$ ,  $\text{P}_2\text{O}_3$  and  $\text{K}_2\text{O}$ . The textural properties of FA, magnetic CS, and CS-FA/ $\text{Fe}_3\text{O}_4$  composite are presented in Table 4. The BET surface area analysis (Table 4) shows that the FA has surface area 4.74 ( $\text{m}^2/\text{g}$ ), while BET surface area of magnetic CS and CS-FA/ $\text{Fe}_3\text{O}_4$  composite were 2.22  $\text{m}^2/\text{g}$  and 8.57  $\text{m}^2/\text{g}$ , respectively. The results reflect a relatively high surface area of CS-FA/ $\text{Fe}_3\text{O}_4$  composite compared to CS/ $\text{Fe}_3\text{O}_4$  which can be attributed to the interfacial interaction between FA and the molecular structure of CS [37]. Furthermore, CS-FA/ $\text{Fe}_3\text{O}_4$  composite is a mesoporous material in accordance with the classification of IUPAC (USA) [38]. The potentiometric titrations showed the CS/ $\text{Fe}_3\text{O}_4$  has 45.6% amino group ( $-\text{NH}_2$ ) content, while CS-FA/ $\text{Fe}_3\text{O}_4$  composite was 39.5%. The decreasing in amine ( $-\text{NH}_2$ ) content of the matrix of CS after incorporation of FA particles can be attributed to the physical loading of FA into molecular structure of CS/ $\text{Fe}_3\text{O}_4$ , and also to the chemical interactions between silicon matrix and/or negative charge of FA with basic sites of amino group in CS molecular structure [39]. The results indicate that CS-FA/ $\text{Fe}_3\text{O}_4$  composite has a relatively high content of amino ( $-\text{NH}_2$ ) group. The protonation of amino ( $-\text{NH}_2$ ) group into ( $-\text{NH}_3^+$ ) in acidic environment can play an important role in the adsorption of RO16 dye due to electrostatic attraction between cationic amino groups ( $-\text{NH}_3^+$ ) of CS-FA/ $\text{Fe}_3\text{O}_4$  composite and RO16 dye anions.

**Table 3** XRF analysis for FA sample

Element	Conc.	Unit
Al	0.94	%
Si	4.71	%
P	0.32	%
K	0.98	%
Ca	2.01	%
Ti	1.08	%
Fe	5.07	%
Sr	0.29	%
Zr	0.18	%
Ag	0.12	%

**Table 4** Textural properties of FA, CS/ $\text{Fe}_3\text{O}_4$ , and CS-FA/ $\text{Fe}_3\text{O}_4$  composite

Sample name	BET surface area ( $\text{m}^2/\text{g}$ )	Mean pore diameter (nm)
FA	4.74	6.62
CS/ $\text{Fe}_3\text{O}_4$	2.22	49.5
CS-FA/ $\text{Fe}_3\text{O}_4$	8.57	7.84

#### XRD Analysis

The XRD pattern of the FA was given in Fig. 2. The FA profile shows sharp peaks at  $2\theta = 16^\circ$ ,  $22^\circ$ ,  $26^\circ$ ,  $33^\circ$ ,  $39^\circ$ ,  $41^\circ$ ,  $50^\circ$ ,  $60^\circ$ ,  $61^\circ$ , and  $68^\circ$ . These peaks reflect that the FA consisted primarily of crystalline phases like alumina ( $\text{Al}_2\text{O}_3$ ), quartz ( $\text{SiO}_2$ ), and hematite ( $\text{Fe}_2\text{O}_3$ ) [40]. The XRD pattern of CS/ $\text{Fe}_3\text{O}_4$  shows sharp characteristic peaks at  $2\theta = 30^\circ$ ,  $35^\circ$ ,  $43^\circ$ ,  $53^\circ$ ,  $57^\circ$ , and  $62^\circ$ , which are consistent with the

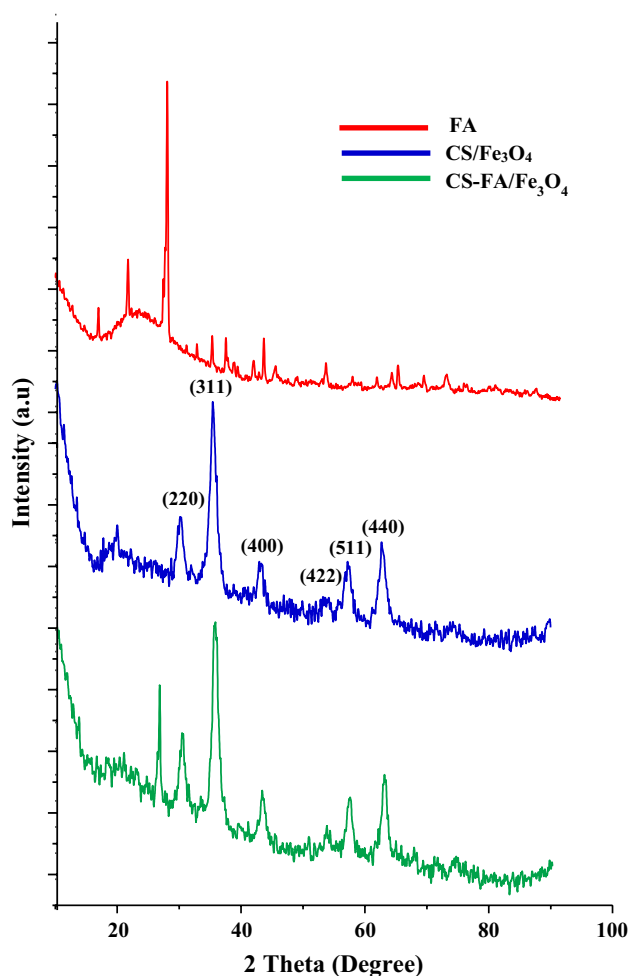


**Fig. 2** XRD patterns of **a** FA, **b** CS/ $\text{Fe}_3\text{O}_4$ , and **c** CS-FA/ $\text{Fe}_3\text{O}_4$  composite

peaks of the  $\text{Fe}_3\text{O}_4$  standard cards (JCPDS file No. 19-629) for the (220), (311), (400), (422), (511), and (440) crystal surfaces, respectively [41]. The XRD pattern of CS-FA/ $\text{Fe}_3\text{O}_4$  composite shows similar profile to the CS/ $\text{Fe}_3\text{O}_4$ , except a sharp peak related to FA was appeared in pattern of CS-FA/ $\text{Fe}_3\text{O}_4$  composite with obvious shift from  $2\theta = 26^\circ$  to  $2\theta = 27^\circ$ , indicating a successful interaction between FA and CS/ $\text{Fe}_3\text{O}_4$ .

### FTIR Analysis

FTIR spectra of FA, CS-FA/ $\text{Fe}_3\text{O}_4$  composite, and CS-FA/ $\text{Fe}_3\text{O}_4$  composite after adsorption of RO16 dye are presented in Fig. 3. The FTIR spectrum of FA displayed characteristic peaks at  $1070\text{ cm}^{-1}$  and  $790\text{ cm}^{-1}$  for bond stretching of asymmetric Si–O–Si and symmetric Si–O–Si, respectively [23]. The peaks in region between  $3600$  and  $3770\text{ cm}^{-1}$  indicates the stretching vibrations of OH [42]. The FTIR

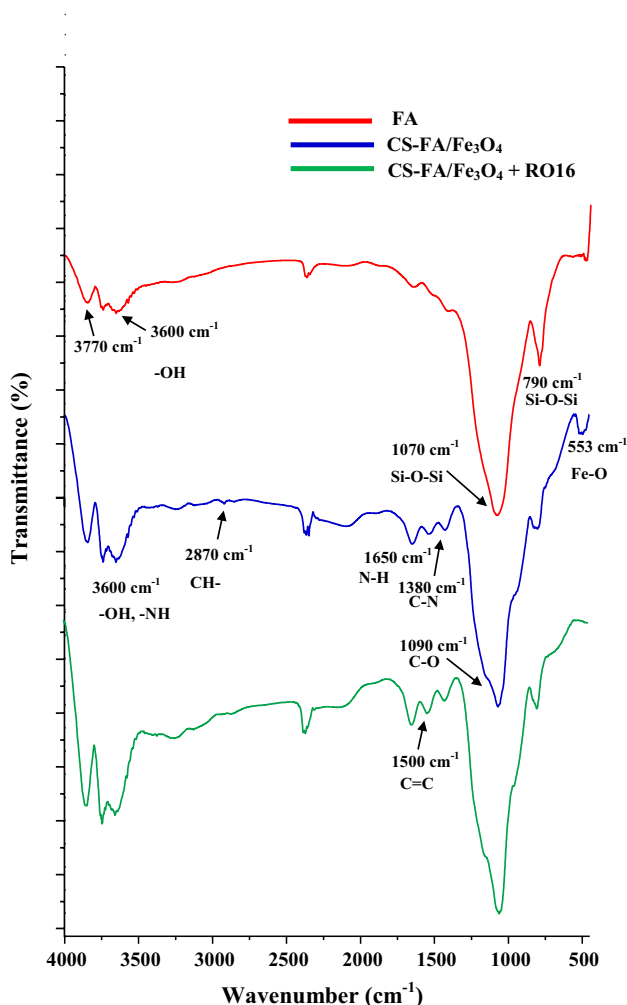


**Fig. 3** FTIR spectra of **a** FA, **b** CS-FA/ $\text{Fe}_3\text{O}_4$  composite, and **c** CS-FA/ $\text{Fe}_3\text{O}_4$  composite after adsorption of RO16 dye

spectrum of CS-FA/ $\text{Fe}_3\text{O}_4$  composite showed major bands for CS polymer which can be assigned as follows:  $3600\text{ cm}^{-1}$  (stretching vibrations of –NH and –OH bonds),  $2870\text{ cm}^{-1}$  (stretching vibrations of C–H in –CH and –CH<sub>2</sub>),  $1650\text{ cm}^{-1}$  (bending vibration of N–H),  $1380\text{ cm}^{-1}$  (stretching vibration of C–N), and  $1090\text{ cm}^{-1}$  (skeletal vibration of C–O) [37]. The peak at  $553\text{ cm}^{-1}$  corresponds to Fe–O bond [43]. The FTIR spectrum of CS-FA/ $\text{Fe}_3\text{O}_4$  composite after adsorption of RO16 dye did not show much difference in bands position compare to spectrum of CS-FA/ $\text{Fe}_3\text{O}_4$  composite before RO16 dye adsorption, except slight shifting of some bands due to involvement the functional groups of CS-FA/ $\text{Fe}_3\text{O}_4$  composite in the RO16 dye adsorption process. Furthermore, the band at  $1500\text{ cm}^{-1}$  can be attributed to the aromatic rings (C=C) of RO16 dye adsorbed on the surface of CS-FA/ $\text{Fe}_3\text{O}_4$  composite.

### SEM–EDX Analysis

SEM–EDX analysis was carried out in order to investigate the surface morphological structure of FA, CS/ $\text{Fe}_3\text{O}_4$ , CS-FA/ $\text{Fe}_3\text{O}_4$  composite, and CS-FA/ $\text{Fe}_3\text{O}_4$  composite after adsorption of RO16 dye along with chemical composition. Figure 4a–d shows the SEM images and EDX analysis of FA, CS/ $\text{Fe}_3\text{O}_4$ , CS-FA/ $\text{Fe}_3\text{O}_4$  composite and CS-FA/ $\text{Fe}_3\text{O}_4$  composite after adsorption of RO16 dye, respectively. Figure 4a shows that the fly ash particles in different particle sizes were clearly visible in spherical shape (as highlighted in red cycles) with regular and smooth surface. The EDX analysis shows that the FA contains the elements C, O, Al and Si. In fact, the presence of C element within the elements of the analysis of EDX indicates to presence of unburned carbon, which plays an important role in adsorption process [44]. The surface morphology of CS/ $\text{Fe}_3\text{O}_4$  (Fig. 4b) shows regular, compact, and homogenous surface, indicating equal distribution of magnetic  $\text{Fe}_3\text{O}_4$  particles into molecular structure of CS. The EDX analysis shows that the CS/ $\text{Fe}_3\text{O}_4$  contains the elements of CS biopolymer such as C, O, and N, in addition to presence element Fe corresponds to the magnetic  $\text{Fe}_3\text{O}_4$ . The surface morphology of CS-FA/ $\text{Fe}_3\text{O}_4$  composite as shown in Fig. 4c appeared as irregular and heterogeneous surface with many visible cavities and pores. The appearance of spherical particles in the image indicates successful incorporation FA particles into molecular structure of CS. The EDX analysis shows a slight decrease in the elemental content of C which can be attributed to the loading of FA into molecular structure of CS/ $\text{Fe}_3\text{O}_4$ . The surface of CS-FA/ $\text{Fe}_3\text{O}_4$  after the adsorption of RO16 dye (Fig. 4d) was turned to be less porous with evanescence of crevices on the CS-FA/ $\text{Fe}_3\text{O}_4$  surface, indicating the RO16 dye molecules adsorbed on the CS-FA/ $\text{Fe}_3\text{O}_4$  surface. The EDX analysis shows the presence of S

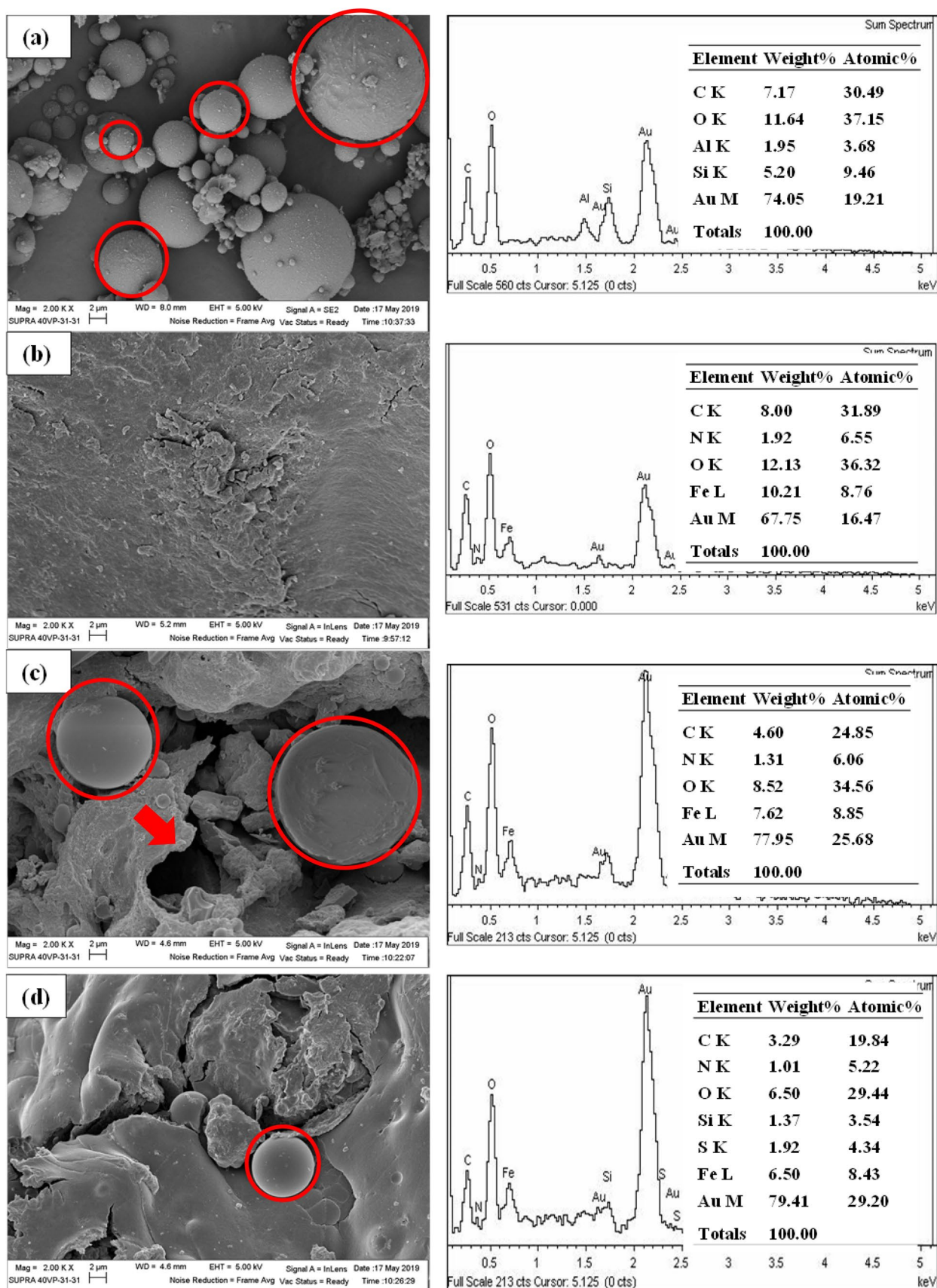


Fig. 4 SEM images and EDX spectra of **a** FA, **b** CS/Fe<sub>3</sub>O<sub>4</sub>, **c** CS-FA/Fe<sub>3</sub>O<sub>4</sub> composite, and **d** CS-FA/Fe<sub>3</sub>O<sub>4</sub> composite after adsorption of RO16 dye

element belongs to RO16 dye and reconfirms the RO16 dye adsorption by CS-FA/Fe<sub>3</sub>O<sub>4</sub> surface.

### BBD Model Analysis

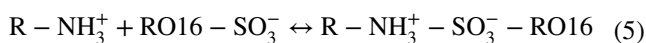
The individual and interactive effects of the independent factors including adsorbent dose (A), solution pH (B), temperature (C) and time (D) on the RO16 dye removal were investigated using BBD-RSM. Analysis of variance (ANOVA) was employed to analyze the experimental results of RO16 dye removal statistically as shown in Table 5. Based on Table 5 (ANOVA analysis), the F-value of model and the corresponding p-value are 17.7 and <0.0001, respectively. These values indicate that the model is statistically significant [45]. The coefficient of determination (*R*<sup>2</sup>) value was close to the unity, indicating to the high correlation between the values of actual and the predicted. Generally, the terms of model with p-value less than 0.05 (Prob > F < 0.0500) are significant on the RO16 dye removal under chosen conditions. According to Table 5, the BBD model terms of A, B, C, E, A<sup>2</sup>, B<sup>2</sup>, C<sup>2</sup>, AD and BC are significant on the RO16 dye removal. However, the terms of BBD model with p-value larger than 0.05 were excluded from second-order polynomial model in order to achieve fitting of the BBD model. Thus, the equation of second-order polynomial model between tested factors and the RO16 dye removal (response) was obtained and described in the following Eq. (4):

$$\begin{aligned} \text{RO16 removal (\%)} = & +15.18 + 8.32A - 15.10B \\ & - 5.83C + 5.96D + 6.78AD \\ & + 13.35BC + 4.74A^2 + 14.66B^2 \\ & + 5.35C^2 \end{aligned} \tag{4}$$

Validation of model can be also achieved by graphical methods through investigation in the nature of residuals distribution of the model, and relationship between values of the predicted and actual RO16 dye removal. Figure 5a shows normal probability plot of residuals for the model. It was observed from Fig. 5a, the perfect normal distributions of the residuals, where points seem conspicuously close to a straight line. This observation indicates to the accuracy of the assumptions and independence of the residuals [46]. The relationship between the values of predicted and actual RO16 dye removal (%) is shown in Fig. 5b which indicates the values of predicted and actual are close to each other, and confirming the statistical validation of the model.

### Interactive Effects of Two Variables on RO16 Dye Removal

The interaction effect between any two independent variables on the RO16 dye removal was evaluated. The interaction effect between solution pH (B) and temperature (C) on the RO16 dye removal was significant (p-value = 0.0002), while the other factors (adsorbent dose 0.08 g and time 55 min) remained constant. The plots of three-dimensional (3D) response surfaces and two dimensional (2D) contour for the impacts and interaction of solution pH (B) and temperature (C) on RO16 dye removal (%) were shown in Fig. 6a, b, respectively. According to Fig. 6a, b can be noticed that the lowering solution pH from 10 to 4 is responsible for increasing the RO16 dye removal (%) from 7.90 to 73.1%. The pH<sub>pzc</sub> value of CS-FA/Fe<sub>3</sub>O<sub>4</sub> composite was 7 as depicted in Fig. 6c. This result elucidates that the CS-FA/Fe<sub>3</sub>O<sub>4</sub> composite has a cationic character and reinforced the availability of the amino (–NH<sub>3</sub><sup>+</sup>) cationic group on the CS-FA/Fe<sub>3</sub>O<sub>4</sub> surface, and in a good agreement with the potentiometric titrations test. The surface of CS-FA/Fe<sub>3</sub>O<sub>4</sub> composite can be converted to positive charge at pH value below the pH<sub>pzc</sub>, thus promoting the adsorption of anions RO16 dye species. As a result, a strong electrostatic interaction can be occurred between protonated amino (–NH<sub>3</sub>) functional group of CS-FA/Fe<sub>3</sub>O<sub>4</sub> composite and sulfonate (–SO<sub>3</sub><sup>–</sup>) groups of the RO16 dye, thus increasing the RO16 dye removal as shown in Eq. (5).



Furthermore, it was observed from Fig. 6a, b the highest RO16 dye removal was achieved at temperature 30 °C,

**Table 5** Analysis of variance (ANOVA) for the removal of RO16 dye

Source	Sum of squares	Df	Mean square	F-value	P-value
Model	6854.35	14	489.60	17.69	<0.0001
A-Adsorbent dose	830.00	1	830.00	30.00	<0.0001
B-pH	2736.12	1	2736.12	98.89	<0.0001
C-Temp	407.17	1	407.17	14.72	0.0018
D-Time	426.02	1	426.02	15.40	0.0015
AB	21.62	1	21.62	0.7815	0.3916
AC	0.81	1	0.81	0.0293	0.8666
AD	183.60	1	183.60	6.64	0.0220
BC	712.89	1	712.89	25.76	0.0002
BD	29.70	1	29.70	1.07	0.3177
CD	1.82	1	1.82	0.0659	0.8012
A <sup>2</sup>	145.43	1	145.43	5.26	0.0379
B <sup>2</sup>	1394.05	1	1394.05	50.38	<0.0001
C <sup>2</sup>	185.49	1	185.49	6.70	0.0214
D <sup>2</sup>	3.62	1	3.62	0.1310	0.7228
Residual	387.37	14	27.67		
Cor Total	7241.72	28			



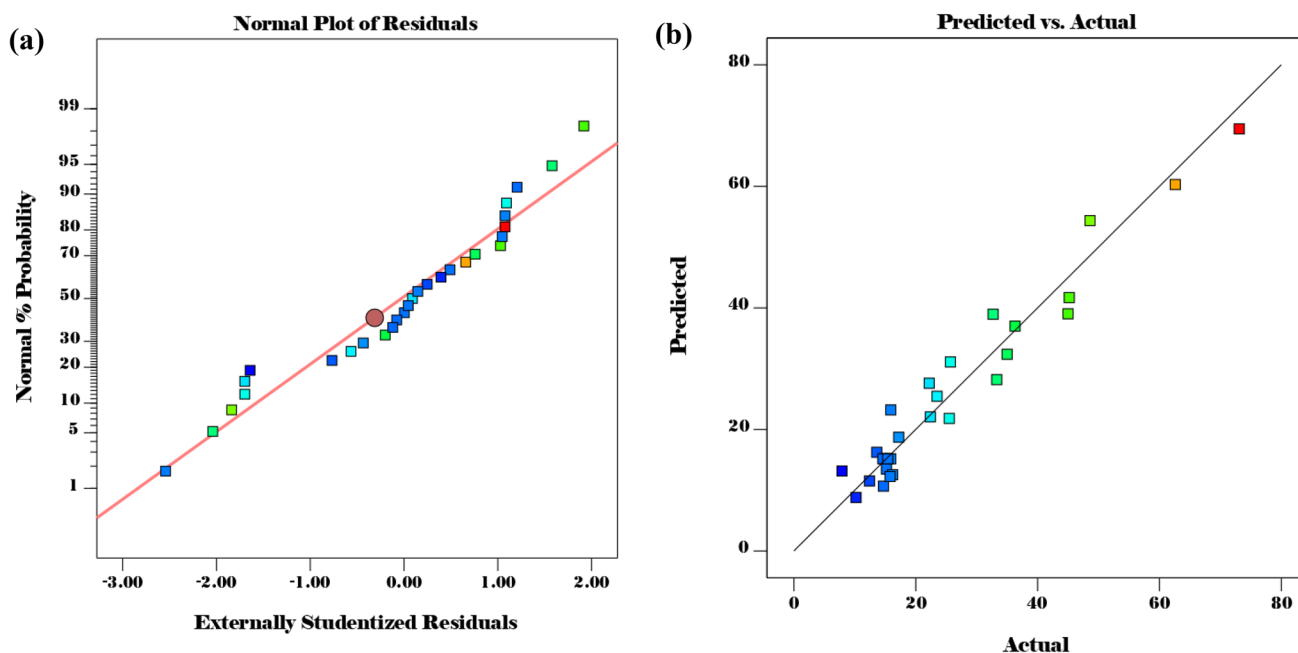


**Fig. 5** **a** Normal probability plot of residuals for BBD model, **b** plot of the relationship between the predicted and actual values of RO16 dye removal (%)

indicating the RO16 dye adsorption process onto the CS-FA/ $\text{Fe}_3\text{O}_4$  surface was an exothermic in nature [47].

Another significant interaction (p-value = 0.022) on the RO16 dye removal (%) was between adsorbent dose (A) and time (D), while the other parameters (solution pH 7 and temperature 40 °C) remained constant. The plots of three-dimensional (3D) response surfaces and two dimensional (2D) contour for the impacts and interaction of adsorbent dose (A) and time (D) on RO16 dye removal (%) were shown in Fig. 6d, e, respectively. As depicted in Fig. 6d, e, the dye removal (%) was gradually increased by increasing adsorbent dose which can be attributed to the increase in the available surface area of CS-FA/ $\text{Fe}_3\text{O}_4$  in dye solution, and also higher CS-FA/ $\text{Fe}_3\text{O}_4$  dose indicates a greater number of active adsorption sites available. Moreover, the RO 16 dye removal was increased by increasing the contact time from 20 to 90 min, with longer contact time the RO16 dye molecules will get sufficient time to move deeper toward inner active adsorption sites on the surface of CS-FA/ $\text{Fe}_3\text{O}_4$ .

### Adsorption Study

The effect of initial RO16 dye concentration and contact time on adsorption equilibrium was investigated. The adsorption capacity,  $q_t$  (mg/g) against time at several initial RO16 concentrations of 20, 40, 60, 80, 100 and 150 mg/L was investigated as depicted in Fig. 7a, while the other optimum factors

like adsorbent dose = 0.08 g, solution pH 4, and temperature = 30 °C were kept constant. It is observed from Fig. 7a that the quantity of RO16 dye molecules uptake onto surface of CS-FA/ $\text{Fe}_3\text{O}_4$  composite raised from 12.4 to 45.7 mg/g by increasing the initial RO16 dye concentrations from 20 to 150 mg/L. This can be attributed to the higher concentration gradient which provides a driving force to move the RO16 molecules towards active adsorption sites [48].

### Adsorption Kinetics

In order to understand the controlling mechanism of the adsorption process of RO16 dye molecules on the CS-FA/ $\text{Fe}_3\text{O}_4$  composite, the non-linear pseudo-first-order (PFO) and non-linear pseudo-second-order (PSO) kinetic models were utilized to analyze the experimental data of the RO16 dye adsorption on CS-FA/ $\text{Fe}_3\text{O}_4$  composite at different initial RO16 dye concentrations [49]. The non-linear equations of the kinetic models PFO [50] and PSO [51] are expressed in Eqs. (6) and (7) as follows:

$$q_t = q_e(1 - \exp^{-k_1 t}) \quad (6)$$

$$q_t = \frac{q_e^2 k_2 t}{1 + q_e k_2 t} \quad (7)$$

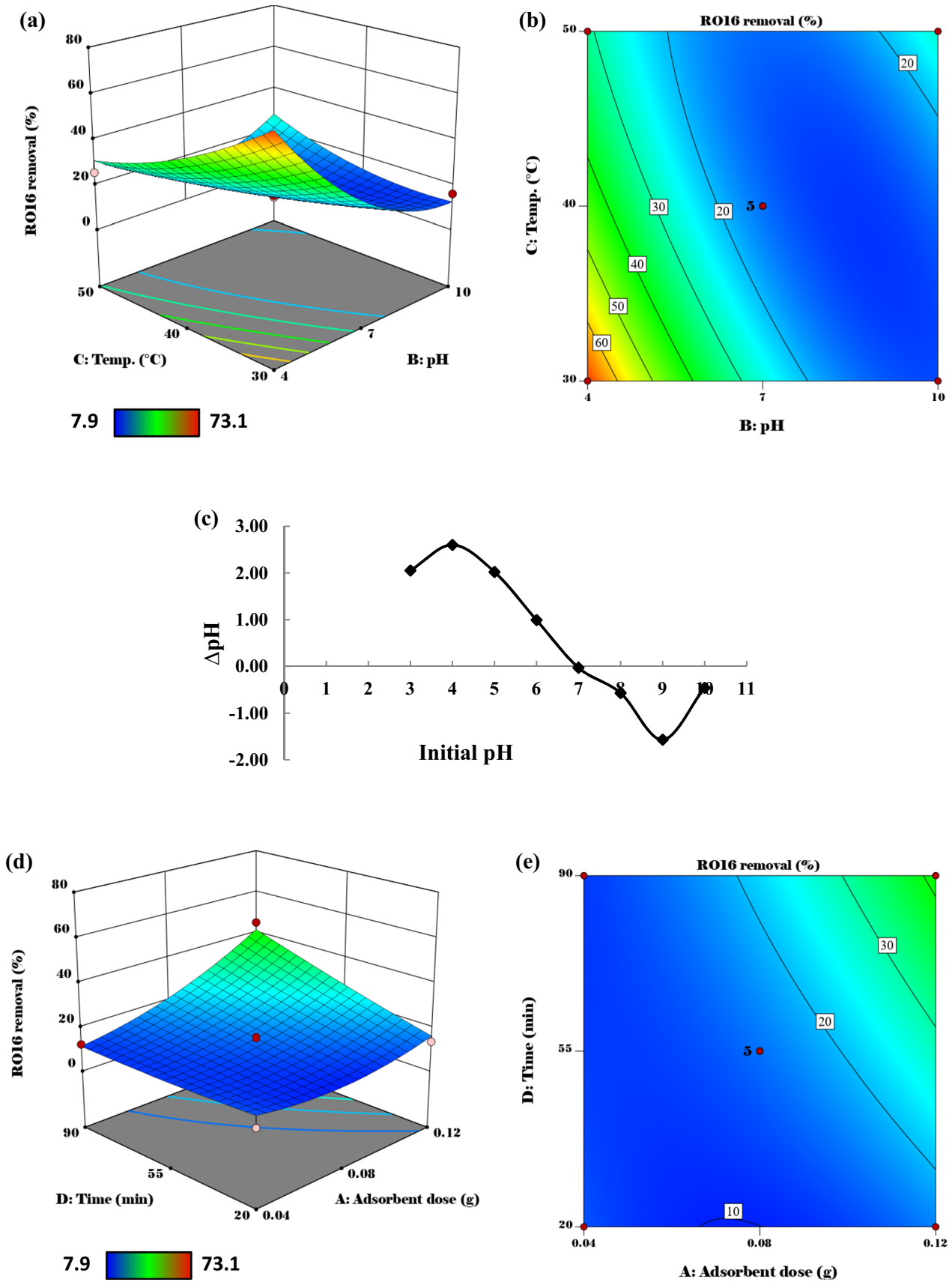


**Fig. 6** **a** 3D response surface plot, **b** contour plot of RO16 dye removal showing the interaction between pH and temperature, **c** pH<sub>PZC</sub> of CS-FA/Fe<sub>3</sub>O<sub>4</sub> composite, and **d** 3D response surface plot, **e** contour plot of RO16 dye removal showing interaction between adsorbent dose and time

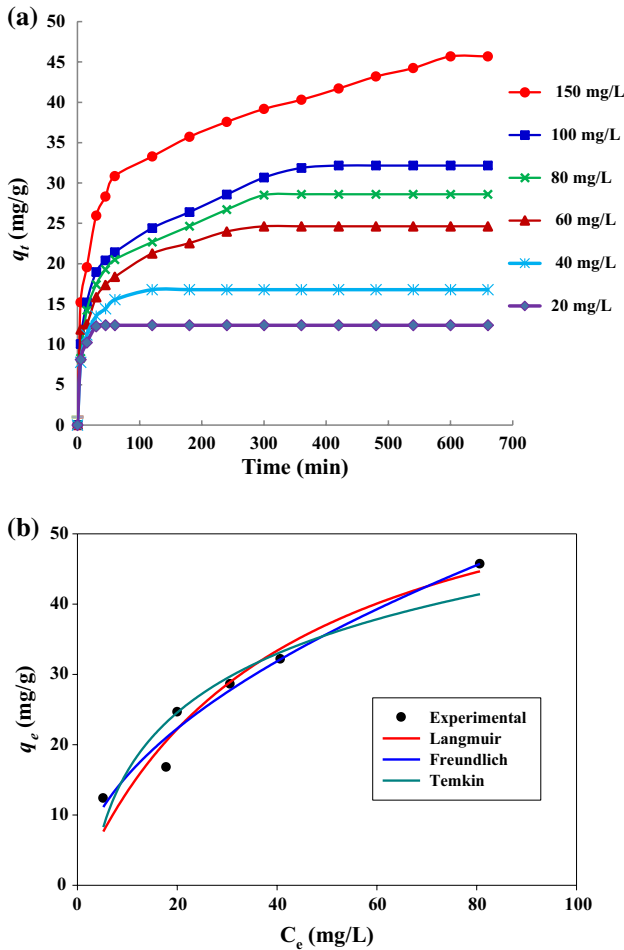


**Fig. 7** **a** Effect of the contact time on RO16 adsorption at different initial concentrations, and **b** adsorption isotherms of RO16 dye by CS-FA/Fe<sub>3</sub>O<sub>4</sub> composite (adsorbent dose = 0.16 g, pH of solution = 4, temperature = 30 °C, agitation speed = 100 strokes and volume of solution = 100 mL)

where,  $q_t$  (mg/g) is the amount of RO16 dye adsorbed at time (t), and  $q_e$  (mg/g) is the amount of RO16 dye adsorbed at equilibrium.  $k_1$  (1/min) is the rate constant of PFO, and  $k_2$  (g/mg min) is the rate constant of PSO. The parameters of kinetic models and  $R^2$  values are recorded in Table 6. According to experimental data (Table 6) can be concluded that the adsorption of RO16 dye molecules by the CS-FA/Fe<sub>3</sub>O<sub>4</sub> composite follows PSO model due to the higher correlation coefficient ( $R^2$ ) values, in addition to the calculated  $q_e$  ( $q_{e,cal}$ ) values fitted well with the experimental  $q_e$  ( $q_{e,exp}$ ) values. This result indicates that the adsorption of RO16 dye by CS-FA/Fe<sub>3</sub>O<sub>4</sub> composite was the chemisorption process involving the electrostatic interaction between the positively charged available on the surface of CS-FA/Fe<sub>3</sub>O<sub>4</sub> composite and the RO16 dye anions [52].

**Adsorption Isotherms**

Adsorption isotherm is essential to understand the interaction between the RO16 dye molecules and the CS-FA/Fe<sub>3</sub>O<sub>4</sub> composite [53, 54]. In order to evaluate the adsorption capacity of CS-FA/Fe<sub>3</sub>O<sub>4</sub> composite for RO16 dye, non-linear equilibrium models of Langmuir, Freundlich, and Temkin were utilized to fit the experimental data. The non-linear equations of the equilibrium models Langmuir [55], Freundlich [56], and Temkin [57] are presented in Eqs. (8), (9), and (10), respectively.

$$q_e = \frac{q_{max}K_a C_e}{1 + K_a C_e} \tag{8}$$

$$q_e = K_f C_e^{1/n} \tag{9}$$

$$q_e = \frac{RT}{b_T} \ln(K_T C_e) \tag{10}$$

where  $q_e$  (mg/g) is the amount of RO16 dye adsorbed at equilibrium,  $C_e$  (mg/L) is the concentration of RO16 dye at equilibrium,  $q_{max}$  (mg/g) is the maximum adsorption capacity, and  $K_a$  (L/mg) is Langmuir constant.  $K_f$  (mg/g) (L/mg)<sup>1/n</sup> is the Freundlich constant,  $n$  is the dimensionless constant

**Table 6** PFO and PSO kinetic parameters for RO16 dye adsorption on CS-FA/Fe<sub>3</sub>O<sub>4</sub> composite

Concentration (mg/L)	$q_{e,exp}$ (mg/g)	PFO			PSO		
		$q_{e,cal}$ (mg/g)	$k_1$ (1/min)	$R^2$	$q_{e,cal}$ (mg/g)	$k_2 \times 10^{-2}$ (g/mg min)	$R^2$
20	12.4	12.2	0.18	0.98	12.5	3.0	0.99
40	16.8	16.4	0.08	0.96	17.1	0.8	0.99
60	24.6	23.7	0.04	0.78	24.7	0.3	0.95
80	28.6	27.3	0.03	0.93	29.1	0.2	0.98
100	32.2	30.2	0.02	0.90	32.3	0.14	0.96
150	45.7	40.5	0.03	0.88	43.4	0.11	0.95

**Table 7** Parameters of the Langmuir, Freundlich, and Temkin isotherm models for RO16 dye adsorption on CS-FA/Fe<sub>3</sub>O<sub>4</sub> composite at 30 °C

Adsorption isotherm	Parameter	Value
Langmuir	$q_m$ (mg/g)	66.9
	$K_a$ (L/mg)	0.02
	$R^2$	0.93
Freundlich	$K_f$ (mg/g) (L/mg) <sup>1/n</sup>	4.76
	$n$	1.94
	$R^2$	0.96
Temkin	$K_T$ (L/mg)	0.96
	$b_T$ (J/mol)	208
	$R^2$	0.88

indicates to the adsorption intensity.  $K_T$  (L/mg) is Temkin constant,  $T$  (K) is temperature,  $R$  (8.314 J/molK) is the universal gas constant, and  $b_T$  (J/mol) is heat of adsorption. The non-linear curves of the equilibrium models are shown in

Fig. 7b. The parameters of equilibrium models are recorded in Table 7. According to the  $R^2$  values (Table 7) obtained from the isotherm models, it observed that the Freundlich isotherm has highest correlation ( $R^2$  0.96), which indicated that the RO16 dye adsorption occurred on heterogeneous surface [58]. The maximum adsorption capacity ( $q_{max}$ ) of CS-FA/Fe<sub>3</sub>O<sub>4</sub> composite for RO16 dye was 66.9 mg/g at 30 °C. It can be deduced that the CS-FA/Fe<sub>3</sub>O<sub>4</sub> composite was a potential and effective biosorbent for removal of RO16 dye from aqueous media.

### Adsorption Mechanism

Adsorption mechanism of RO16 dye on CS-FA/Fe<sub>3</sub>O<sub>4</sub> composite surface by different types of interactions is shown in Fig. 8. An electrostatic attraction (Fig. 8a) is considered from the most interaction that can be occurred between RO16 dye and surface of adsorbent. This mechanism involves the electrostatic interaction between RO16 dye anions with positively charged available on the CS-FA/Fe<sub>3</sub>O<sub>4</sub>

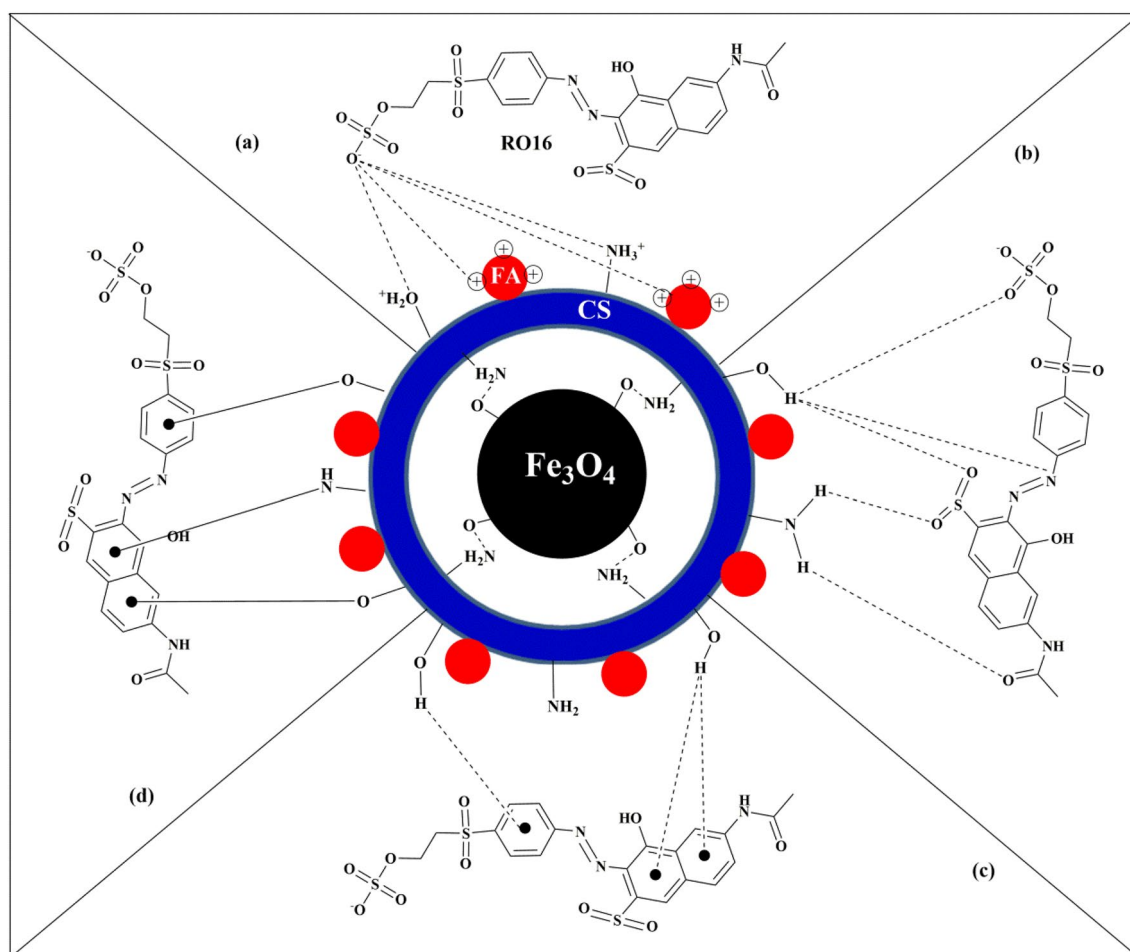


**Fig. 8** Illustration of the possible adsorption mechanism between CS-FA/Fe<sub>3</sub>O<sub>4</sub> composite and RO16 dye: **a** electrostatic attraction, **b** dipole-dipole hydrogen bonding interactions, **c** Yoshida H-bonding, and **d**  $n$ - $\pi$  stacking interactions

composite surface. Adsorption mechanism also includes H-bonding interactions such as dipole–dipole hydrogen bonding (Fig. 8b), and Yoshida H-bonding (Fig. 8c). Dipole–dipole hydrogen bonding happens between H atom available on the surface of CS-FA/Fe<sub>3</sub>O<sub>4</sub> composite, and N atoms in the RO16 dye structure, while Yoshida H-bonding happens between –OH available on the surface of CS-FA/Fe<sub>3</sub>O<sub>4</sub> composite, and the aromatic rings of RO16 dye. [59]. Finally, n–π interaction comes from delocalization of the lone pair electron of O and N atoms into the π orbital of the dye aromatic rings as shown in Fig. 8d [60]. According to the above, it can be concluded that these interactions are effective in enhancing adsorption process of RO16 dye on the surface of CS-FA/Fe<sub>3</sub>O<sub>4</sub> composite.

## Conclusion

Magnetic fly ash/Fe<sub>3</sub>O<sub>4</sub> particles (CS-FA/Fe<sub>3</sub>O<sub>4</sub>) composite was successfully synthesized and applied as an effective bioadsorbent for the removal of RO16. The incorporation of FA particles in magnetic CS leads to enhance surface area of CS-FA/Fe<sub>3</sub>O<sub>4</sub> composite. The CS-FA/Fe<sub>3</sub>O<sub>4</sub> composite was easily separated and collected from the aqueous solution after adsorption process by external magnetic field. Analysis of variance (ANOVA) showed the F-value of model and the corresponding p-value are 17.7 and < 0.0001, indicating the model is statistically significant. The experimental results indicate that the highest RO16 dye removal of 73.1% was observed by significant interaction between BC (pH × temperature, p-value = 0.0002) and AD (adsorbent dose × time, p-value = 0.022). The optimum conditions of adsorption process parameters were pH ~ 4, adsorbent dose (0.08 g), temperature (30 °C) and time (55 min). The kinetics and isotherms models results indicated that the adsorption was affected by chemisorption and heterogeneous mode of adsorption. The  $q_{max}$  of CS-FA/Fe<sub>3</sub>O<sub>4</sub> composite for RO16 dye was 66.9 mg/g at 30 °C.

**Acknowledgements** The authors would like to thank Ministry of Higher Education, Malaysia for supporting this research project under fundamental research Grant scheme (600-IRMI/FRGS5/3 (340/2019); FRGS/1/2019/STG01/UiTM/02/3).

## References

- Ahamad T, Naushad M, Al-Maswari BM, Alshehri SM (2019) Fabrication of highly porous adsorbent derived from bio-based polymer metal complex for the remediation of water pollutants. *J Clean Prod* 208:1317–1326
- Abdulhameed AS, Mohammad AT, Jawad AH (2019) Modeling and mechanism of reactive orange 16 dye adsorption by chitosan-glyoxal/ TiO<sub>2</sub> nanocomposite: application of response surface methodology. *Desalin Water Treat* 164:346–360
- Alansi AM, Al-Qunaibit M, Alade IO, Qahtan TF, Saleh TA (2018) Visible-light responsive BiOBr nanoparticles loaded on reduced graphene oxide for photocatalytic degradation of dye. *J Mol Liq* 253:297–304
- Agnihotri S, Singhal R (2019) Effect of sodium alginate content in acrylic acid/sodium humate/sodium alginate superabsorbent hydrogel on removal capacity of MB and CV dye by adsorption. *J Polym Environ* 27(2):372–385
- Jawad AH, Mubarak NSA, Abdulhameed AS (2020) Hybrid crosslinked Chitosan epichlorohydrin/TiO<sub>2</sub> nanocomposite for reactive red 120 dye adsorption: kinetic, isotherm, thermodynamic, and mechanism study. *J Polym Environ* 28:624–637
- Nidheesh PV, Zhou M, Oturan MA (2018) An overview on the removal of synthetic dyes from water by electrochemical advanced oxidation processes. *Chemosphere* 197:210–227
- Beluci NDCL, Mateus GAP, Miyashiro CS, Homem NC, Gomes RG, Fagundes-Klen MR, Vieira AMS (2019) Hybrid treatment of coagulation/flocculation process followed by ultrafiltration in TiO<sub>2</sub>-modified membranes to improve the removal of reactive black 5 dye. *Sci Total Environ* 664:222–229
- Jawad AH, Waheeb AS, Rashid RA, Nawawi WI, Yousif E (2018) Equilibrium isotherms, kinetics, and thermodynamics studies of methylene blue adsorption on pomegranate (*Punica granatum*) peels as a natural low-cost biosorbent. *Desalin Water Treat* 105:322–331
- Saleh TA, Al-Absi AA (2017) Kinetics, isotherms and thermodynamic evaluation of amine functionalized magnetic carbon for methyl red removal from aqueous solutions. *J Mol Liq* 248:577–585
- Saleh TA (2015) Mercury sorption by silica/carbon nanotubes and silica/activated carbon: a comparison study. *J Water Supply Res Technol* 64(8):892–903
- Tanhaei B, Ayati A, Sillanpää M (2019) Magnetic xanthate modified chitosan as an emerging adsorbent for cationic azo dyes removal: Kinetic, thermodynamic and isothermal studies. *Int J Biol Macromol* 121:1126–1134
- Wu J, Cheng X, Yang G (2019) Preparation of nanochitin-contained magnetic chitosan microfibers via continuous injection gelation method for removal of Ni (II) ion from aqueous solution. *Int J Biol Macromol* 125:404–413
- Abdulhameed AS, Jawad AH, Mohammad AT (2019) Synthesis of chitosan-ethylene glycol diglycidyl ether/TiO<sub>2</sub> nanoparticles for adsorption of reactive orange 16 dye using a response surface methodology approach. *Bioresour Technol* 293:122071
- Jawad AH, Nawi MA (2012) Characterizations of the photocatalytically-oxidized cross-linked chitosan-glutaraldehyde and its application as a sub-layer in the TiO<sub>2</sub>/CS-GLA bilayer photocatalyst system. *J Polym Environ* 20:817–829
- Saleh TA, Sari A, Tuzen M (2016) Chitosan-modified vermiculite for As (III) adsorption from aqueous solution: equilibrium, thermodynamic and kinetic studies. *J Mol Liq* 219:937–945
- Lai KC, Hiew BYZ, Lee LY, Gan S, Thangalazhy-Gopakumar S, Chiu WS, Khiew PS (2019) Ice-templated graphene oxide/chitosan aerogel as an effective adsorbent for sequestration of metanil yellow dye. *Bioresour Technol* 274:134–144
- Okudan A, Ataoglu BE, Sengoz O, Arslan G (2019) Cu (II) Sorption Performance of Novel Chitosan/Ter-(vinyl pivalate-maleic anhydride-N-tert-butylacrylamide) Microcapsules. *J Polym Environ* 27(11):2454–2463
- Jawad AH, Mamat NH, Hameed BH, Ismail K (2019) Biofilm of cross-linked chitosan-ethylene glycol diglycidyl ether for removal of reactive red 120 and methyl orange: adsorption and mechanism studies. *J Environ Chem Eng* 7(2):102965

19. Mohammad AT, Abdulhameed AS, Jawad AH (2019) Box-Behnken design to optimize the synthesis of new crosslinked chitosan-glyoxal/TiO<sub>2</sub> nanocomposite: methyl orange adsorption and mechanism studies. *Int J Biol Macromol* 129:98–109
20. Jawad AH, Mubarak NSA, Abdulhameed AS (2020) Tunable Schiff's base-cross-linked chitosan composite for the removal of reactive red 120 dye: adsorption and mechanism study. *Int J Biol Macromol* 142:732–741
21. Abdulhameed AS, Mohammad AT, Jawad AH (2019) Application of response surface methodology for enhanced synthesis of chitosan tripolyphosphate/TiO<sub>2</sub> nanocomposite and adsorption of reactive orange 16 dye. *J Clean Prod* 232:43–56
22. Kausar A, Naeem K, Hussain T, Bhatti HN, Jubeen F, Nazir A, Iqbal M (2019) Preparation and characterization of chitosan/clay composite for direct Rose FRN dye removal from aqueous media: comparison of linear and non-linear regression methods. *J Mater Res Technol* 8(1):1161–1174
23. Adamczuk A, Kołodziejka D (2015) Equilibrium, thermodynamic and kinetic studies on removal of chromium, copper, zinc and arsenic from aqueous solutions onto fly ash coated by chitosan. *Chem Eng J* 274:200–212
24. Moradian M, Hu Q, Aboustait M, Robertson B, Ley MT, Hanan JC, Xiao X (2019) Direct in-situ observation of early age void evolution in sustainable cement paste containing fly ash or limestone. *Compos B* 175:107099
25. Ahmaruzzaman M (2010) A review on the utilization of fly ash. *Prog Energy Combust Sci* 36(3):327–363
26. Visa M, Duta A (2013) Methyl-orange and cadmium simultaneous removal using fly ash and photo-Fenton systems. *J Hazard Mater* 244:773–779
27. Agarwal S, Rajoria P, Rani A (2018) Adsorption of tannic acid from aqueous solution onto chitosan/NaOH/fly ash composites: equilibrium, kinetics, thermodynamics and modeling. *J Environ Chem Eng* 6(1):1486–1499
28. Atun G, Ayar N, Kurtoğlu AE, Ortabay S (2019) A comparison of sorptive removal of anthraquinone and azo dyes using fly ash from single and binary solutions. *J Hazard Mater* 371:94–107
29. Yan Y, Yuvaraja G, Liu C, Kong L, Guo K, Reddy GM, Zyryanov GV (2018) Removal of Pb (II) ions from aqueous media using epichlorohydrin crosslinked chitosan Schiff's base@ Fe<sub>3</sub>O<sub>4</sub> (ECCSB@Fe<sub>3</sub>O<sub>4</sub>). *Int J Biol Macromol* 117:1305–1313
30. Saleh TA, Tuzen M, Sari A (2019) Magnetic vermiculite-modified by poly (trimesoyl chloride-melamine) as a sorbent for enhanced removal of bisphenol A. *J Environ Chem Eng* 7(6):103436
31. Liang XX, Omer AM, Hu ZH, Wang YG, Yu D, Ouyang XK (2019) Efficient adsorption of diclofenac sodium from aqueous solutions using magnetic amine-functionalized chitosan. *Chemosphere* 217:270–278
32. Tahira I, Aslam Z, Abbas A, Monim-ul-Mehboob M, Ali S, Asghar A (2019) Adsorptive removal of acidic dye onto grafted chitosan: a plausible grafting and adsorption mechanism. *Int J Biol Macromol* 136:1209–1218
33. Zhou X, Dong C, Yang Z, Tian Z, Lu L, Yang W, Chen J (2018) Enhanced adsorption of pharmaceuticals onto core-brush shaped aromatic rings-functionalized chitosan magnetic composite particles: effects of structural characteristics of both pharmaceuticals and brushes. *J Clean Prod* 172:1025–1034
34. Subedi N, Lähde A, Abu-Danso E, Iqbal J, Bhatnagar AA (2019) Comparative study of magnetic chitosan (Chi@Fe<sub>3</sub>O<sub>4</sub>) and graphene oxide modified magnetic chitosan (Chi@Fe<sub>3</sub>O<sub>4</sub>/GO) nanocomposites for efficient removal of Cr (VI) from water. *Int J Biol Macromol* 137:948–959
35. Vieira RS, Beppu MM (2006) Interaction of natural and crosslinked chitosan membranes with Hg (II) ions. *Colloids Surf A Physicochem Eng Asp* 279(1–3):196–207
36. Dalvand A, Nabizadeh R, Ganjali MR, Khoobi M, Nazmara S, Mahvi AH (2016) Modeling of Reactive Blue 19 azo dye removal from colored textile wastewater using L-arginine-functionalized Fe<sub>3</sub>O<sub>4</sub> nanoparticles: optimization, reusability, kinetic and equilibrium studies. *J Magn Magn Mater* 404:179–189
37. Pandey S, Tiwari S (2015) Facile approach to synthesize chitosan based composite—characterization and cadmium (II) ion adsorption studies. *Carbohydr Polym* 134:646–656
38. Sing KS (1985) Reporting physisorption data for gas/solid systems with special reference to the determination of surface area and porosity (Recommendations 1984). *Pure Appl Chem* 57(4):603–619
39. Wen Y, Tang Z, Chen Y, Gu Y (2011) Adsorption of Cr (VI) from aqueous solutions using chitosan-coated fly ash composite as biosorbent. *Chem Eng J* 175:110–116
40. Singh K, Gupta AB, Sharma AK (2016) Fly ash as low cost adsorbent for treatment of effluent of handmade paper industry-Kinetic and modelling studies for direct black dye. *J Clean Prod* 112:1227–1240
41. Abdelwahab NA, Ghoneim AM (2018) Photocatalytic activity of ZnO coated magnetic crosslinked chitosan/polyvinyl alcohol microspheres. *Mat Sci Eng B* 228:7–17
42. Patra G, Barnwal R, Behera SK, Meikap BC (2018) Removal of dyes from aqueous solution by sorption with fly ash using a hydrocyclone. *J Environ Chem Eng* 6(4):5204–5211
43. Karaer H, Kaya İ (2017) Synthesis, characterization and using at the copper adsorption of chitosan/polyvinyl alcohol magnetic composite. *J Mol Liq* 230:152–162
44. Hower JC, Groppo JG, Graham UM, Ward CR, Kostova IJ, Maroto-Valer MM, Dai S (2017) Coal-derived unburned carbons in fly ash: a review. *Int J Coal Geol* 179:11–27
45. Qu J, Meng X, You H, Ye X, Du Z (2017) Utilization of rice husks functionalized with xanthates as cost-effective biosorbents for optimal Cd (II) removal from aqueous solution via response surface methodology. *Bioresour Technol* 241:1036–1042
46. Natarajan E, Ponnaiah GP (2017) Optimization of process parameters for the decolorization of Reactive Blue 235 dye by barium alginate immobilized iron nanoparticles synthesized from aluminum industry waste. *Environ Nanotechnol Monit Manage* 7:73–88
47. Çelekli A, Al-Nuaimi AI, Bozkurt H (2019) Adsorption kinetic and isotherms of reactive red 120 on *Moringa oleifera* seed as an eco-friendly. *Process J Mol Struct* 1195:168–178
48. Jawad AH, Abdulhameed AS (2020) Mesoporous Iraqi red kaolin clay as an efficient adsorbent for methylene blue dye: adsorption kinetic, isotherm and mechanism study. *Surf Interface* 18:100422
49. Saleh TA (2015) Isotherm, kinetic, and thermodynamic studies on Hg (II) adsorption from aqueous solution by silica-multiwall carbon nanotubes. *Environ Sci Pollut Res* 22(21):16721–16731
50. Lagergren S (1898) Zur theorie der sogenannten adsorption gelöster stoffe. *Vet Akad Handl* 24:1–39
51. Ho YS, McKay G (1998) Sorption of dye from aqueous solution by peat. *Chem Eng J* 70(2):115–124
52. Zhang P, Li Y, Cao Y, Han L (2019) Characteristics of tetracycline adsorption by cow manure biochar prepared at different pyrolysis temperatures. *Bioresour Technol* 285:121348
53. Saleh TA, Tuzen M, Sari A (2018) Polyamide magnetic palygorskite for the simultaneous removal of Hg (II) and methyl mercury; with factorial design analysis. *J Environ Manage* 211:323–333
54. Saleh TA, Tuzen M, Sari A (2017) Polyethylenimine modified activated carbon as novel magnetic adsorbent for the removal of uranium from aqueous solution. *Chem Eng Res Des* 117:218–227
55. Langmuir I (1918) The adsorption of gases on plane surfaces of glass, mica and platinum. *J Am Chem Soc* 40(9):1361–1403
56. Frensdlich HMF (1906) Over the adsorption in solution. *J Phys Chem* 57:385–471

57. Temkin MI (1940) Kinetics of ammonia synthesis on promoted iron catalysts. *Acta physiochim URSS* 12:327–356
58. Salari M, Dehghani MH, Azari A, Motevalli MD, Shabanloo A, Ali I (2019) High performance removal of phenol from aqueous solution by magnetic chitosan based on response surface methodology and genetic algorithm. *J Mol Liq* 285:146–157
59. Parker HL, Hunt AJ, Budarin VL, Shuttleworth PS, Miller KL, Clark JH (2012) The importance of being porous: polysaccharide-derived mesoporous materials for use in dye adsorption. *RSC Adv* 2(24):8992–8997
60. Singh SK, Das A (2015) The  $n \rightarrow \pi^*$  interaction: a rapidly emerging non-covalent interaction. *Phys Chem Chem Phys* 17(15):9596–9612

**Publisher's Note** Springer Nature remains neutral with regard to jurisdictional claims in published maps and institutional affiliations.